

CHANDRA AND RXTE SPECTRA OF THE BURSTER GS 1826–238

THOMAS W. J. THOMPSON¹, RICHARD E. ROTHSCHILD¹, JOHN A. TOMSICK¹, HERMAN L. MARSHALL²*Draft version February 5, 2008*

ABSTRACT

Using simultaneous observations from the *Chandra X-Ray Observatory* and the *Rossi X-Ray Timing Explorer*, we investigated the low-mass X-ray binary (LMXB) and “clocked burster” GS 1826–238 with the goal of studying its spectral and timing properties. The uninterrupted *Chandra* observation captured 6 bursts (*RXTE* saw 3 of the 6), yielding a recurrence time of 3.54 ± 0.03 hr. Using the proportional counter array on board *RXTE*, we made a probable detection of 611 Hz burst oscillations in the decaying phases of the bursts with an average rms signal amplitude of 4.8%. The integrated persistent emission spectrum can be described as the dual Comptonization of ~ 0.3 keV soft photons by a plasma with $kT_e \sim 20$ keV and $\tau \sim 2.6$ (interpreted as emission from the accretion disk corona), plus the Comptonization of hotter ~ 0.8 keV seed photons by a ~ 6.8 keV plasma (interpreted as emission from or near the boundary layer). We discovered evidence for a neutral Fe K α emission line, and we found interstellar Fe L II and Fe L III absorption features. The burst spectrum can be fit by fixing the disk Comptonization parameters to the persistent emission best-fit values, and adding a blackbody. The temperature of the boundary layer seed photons was tied to the blackbody temperature. The blackbody/seed photon temperature at the peak of the burst is ~ 1.8 keV and returns to ~ 0.8 keV over 200 s. The blackbody radius is consistent with $R_{bb} \approx 10.3\text{--}11.7$ km assuming a distance of 6 kpc, though this value cannot be interpreted as the physical size of the neutron star due to partial covering of the stellar surface by the accretion disk. By accounting for the fraction of the surface that is obscured by the disk as a function of binary inclination, we determined the source distance must actually be near 5 kpc in order for the stellar radius to lie within the commonly assumed range of 10–12 km. The order of magnitude increase in flux at burst peak is seen to cause Compton cooling of the electron plasma surrounding the disk, as the plasma temperature decreases to ~ 3 keV at burst onset, and then slowly returns to the persistent emission value after about 150 s.

Subject headings: X-rays: binaries—X-rays: bursts—X-rays: individual (GS 1826–238)

1. INTRODUCTION

The low-mass X-ray binary (LMXB) GS 1826–238 was discovered with *Ginga* in 1988 (Makino et al. 1988). Due to its temporal and spectral similarities to Cyg X–1 and GX 339–4, the source was originally tentatively classified as a black hole candidate (BHC) (Tanaka 1989). Later optical studies lead to the identification of a $V = 19.3$ mag (and therefore low-mass) optical counterpart (Barret et al. 1995). The companion was subsequently found to have a 2.1 hr modulation (and implied orbital period) and a refined position of $\alpha = 18^{\circ}29'28.^s2$ and $\delta = -23^{\circ}47'49.^s12$ (J2000) (Homer et al. 1998).

The spectral and temporal characteristics that Tanaka (1989) initially used to associate GS 1826–238 with a black hole system were later found to be present in other X-ray bursters (e.g., 4U 1608–522, Yoshida et al. 1993). Moreover, the photon index of its energy spectrum was measured to have a relatively low cut-off energy (~ 58 keV) for a BHC, and was perhaps more indicative of the typically cooler neutron star (NS) hard X-ray spectra (Strickman et al. 1996). X-ray bursts from this source were first conclusively observed with *BeppoSAX* by Ubertini et al. (1997), firmly establishing the source as a NS and strongly suggesting it to be weakly magnetized ($B < 10^{10}$ G).

The periodicity of the type I bursts from GS 1826–238 has been remarkably stable over the span of years (Ubertini et al. 1999). Although quasi-periodic bursting is not unique among LMXBs, such consistency over long durations is indeed un-

usual. The regular intervals between bursts suggest that the accretion rate is stable, that the accreted matter is completely consumed during the bursts, and that the fraction of the stellar surface covered prior to each burst is approximately constant. Investigations of burst recurrence rates and energetics have led to convincing arguments that type I bursts stem from unstable thermonuclear burning of accreted hydrogen and helium (e.g., Strohmayer & Bildsten 2003). As freshly accreted material falls onto the NS surface, it is hydrostatically compressed by new material at a rate per unit area $\dot{m} \sim 10^4$ g cm $^{-2}$ s $^{-1}$, assuming isotropic accretion and a NS radius of 10 km. The thermal energy deposited by the infalling matter causes temperatures in most of the thin NS “atmosphere” to exceed 10^7 K, so that during the accumulation phase hydrogen burns via the hot CNO cycle at a rate that is limited only by the mass fraction Z_{CNO} and not the temperature (Bildsten 2000). Within hours to days, the extreme gravity on the NS surface ($\sim 10^{14}$ cm s $^{-2}$) compresses the accumulated matter to densities high enough to trigger unstable thermonuclear ignition. GS 1826–238, in particular, has near limit-cycle behavior with stable hydrogen burning during the accumulation phase followed by mixed hydrogen and helium burning triggered by thermally unstable helium ignition (Bildsten 2000). The α -parameter – the ratio of the integrated persistent fluence between bursts to the burst fluence – and the long burst duration (~ 150 s), imply that after thermonuclear ignition the hydrogen burns via the rapid-proton (*rp*) process where energy is released through successive proton captures and β decays (Wallace & Woosley 1981). The measured α -value for GS 1826–238 of ~ 42 (Galloway et al. 2004; hereafter G04) is remarkably consistent with theoretical predictions: The gravitational energy released during accretion onto a $1.4 M_{\odot}$ NS is about

¹ Center for Astrophysics and Space Sciences, University of California, San Diego, La Jolla, CA 92093; email: tthompson@physics.ucsd.edu

² Center for Space Research, 77 Vassar Street, Massachusetts Institute of Technology, Cambridge, MA 02139

200 MeV per nucleon, while the energy released through thermonuclear fusion is about 5 MeV per nucleon for a solar mix going to iron group elements, giving an expected value of 40. Moreover, the variation in α with the global accretion rate \dot{M} implies solar metallicity in the accreted layer (G04), although recent work using an adaptive nuclear reaction network shows that the critical mass required for a burst is independent of the composition of the accreted material (Woosley et al. 2004), and so attempts to infer the metallicity of the fuel from burst properties is complicated.

During accretion the gravitational potential energy released per nucleon is deposited partly in the disk, and partly in the boundary layer or on the NS surface. In low accretion rate (atoll) LMXBs, the dominant persistent emission spectral component is clearly inverse Comptonization, where soft “seed” photons emitted from a cold layer in the accretion disk gain energy in successive scatterings with hot electrons in the disk or surrounding accretion disk corona (ADC) (Church 2001). Stable hydrogen burning between bursts and the thermal energy released on impact are observable as blackbody emission, assuming there is an optical path through which the radiation can escape. The addition of a blackbody component in spectral models is not always necessary (as we find in § 4), which suggests this form of radiation is (up)scattered or absorbed by the obscuring disk or ADC. Another possibility is that the blackbody component is simply too weak to be observed relative to the Comptonized emission.

Mitsuda et al. (1989) proposed that most LMXB spectra can be described by a multi-temperature disk blackbody from the inner accretion disk plus blackbody emission from the NS which is Comptonized in the local region of the star. More recently, the dipping class of LMXBs has constrained the types of emission models that are most likely. The constraints are provided by the fact that the models must fit the persistent emission at various levels of decreased flux resulting from partial occultation and absorption of the NS, accretion disk, and corona by the bulge in the outer disk where accretion flow from the companion star impacts. The evolution of these spectra at various levels of flux are well-described by a model consisting of point-like blackbody emission plus Comptonized emission from an extended accretion disk corona (e.g., Church et al. 1997, 1998; Bałucińska-Church et al. 2001; Smale et al. 2001). During dipping, the blackbody component is observed to disappear rapidly, indicating that the emission comes from a point and not from an extended region. As expected, the Comptonized component is observed to gradually decrease. By measuring the ingress times of the dip, Church (2001) was able to estimate the size of the Comptonizing region for several sources and found the radius of the region to be typically $\sim 50,000$ km. This measurement is consistent with the value obtained much earlier by Canizares (1976) for 3U 1820–30. The large extent of the emission region is evidence for a Comptonized component that is emitted from an ADC and not the disk itself. Moreover, Smale et al. (2001) observed complete covering of this region in many sources, suggesting that the corona must be geometrically thin, as it would be unlikely that a corona with spherical geometry would be completely occulted. On the contrary, studies of emission and absorption features in dipping sources by Boirin et al. (2005) show that the spectra are also consistent with a less strongly ionized absorber along the line of sight rather than a simple increase in absorption. Progressive covering of the Comptonized component in their

models is not required.

The persistent emission spectrum of GS 1826–238 has been discussed by previous authors (e.g., Barret et al. 1995, Ubertini et al. 1999, Del Sordo et al. 1999, in ’t Zand et al. 1999a, Barret et al. 2000, Kong et al. 2000). The spectral model that has consistently produced an acceptable fit is a blackbody plus Comptonized emission, the latter being modeled in XSPEC with either a cut-off power law (`cutoffpl`) or the more explicit `comptt`. Broadband *BeppoSAX* spectra in the 0.1–200 keV range found the spectrum to be consistent with the Comptonization of a 0.6 keV Wien spectrum by a plasma with $kT_e \sim 20.7$ keV, plus a 3.8 keV blackbody (in ’t Zand et al. 1999a). Del Sordo et al. (1999) found the spectrum to be well-fitted with a blackbody plus cut-off power law, with $kT_{bb} \sim 0.9$ keV, $\Gamma \sim 1.3$, and cut-off energy ~ 50 keV. Strickman et al. (1996) and in ’t Zand et al. (1999a) also obtained a fit with this model and the results of each group are fairly consistent. Kong et al. (2000) fit the persistent emission spectrum from 0.5–10 keV with a blackbody (~ 0.7 keV) plus power law ($\Gamma \sim 1.1$).

The burst emission spectrum has been studied a few times previously. in ’t Zand et al. (1999a) studied burst spectra and found significant flux up to 60 keV, indicating that the burst emission may be Comptonized in a similar manner as the persistent emission. The peak blackbody temperature was measured to be ~ 2 keV, which cooled to about 1.3 keV over 100 s. Ubertini et al. (1999) studied the spectrum for two bursts, though with only two separate integration bins of 13 s at burst peak and 43 s through the decay. The peak spectrum was fit with a blackbody temperature of ~ 2.1 – 2.3 keV and the decay with temperature ~ 1.6 – 1.9 keV. Kong et al. (2000) fit the burst spectrum by fixing the power law component to its persistent value and adding a blackbody; the peak temperature was ~ 2.6 keV. Marshall et al. (2003) searched the present data for absorption features during the burst peak and decay to search for evidence for the gravitational redshift to the surface of the NS. No features were observed.

We begin in § 2 by presenting the observations of GS 1826–238 that were used in this study, and we specifically discuss the data preparation prior to spectral analysis. In § 3 we measure the burst periodicity and compare to previous measurements. We use the burst recurrence time and energetics to discuss the type of burning occurring on the NS surface. We conclude the section by discussing a probable detection of burst oscillations during the decaying phases of the burst. In § 4 we examine the evolution of the broadband persistent emission spectrum between bursts to see whether or not any significant changes in the parameters occur during the accumulation phase. We find that the persistent emission data from 0.5–200 keV are best fit with a model characterized by absorbed emission from two distinct Comptonizing regions, plus iron line emission. We also report the detection of interstellar absorption features. We study the evolution of the burst spectrum in § 5 by adding a blackbody to the persistent emission spectrum. The disk Comptonization parameters are fixed at their persistent emission best-fit values, and the temperature of the boundary layer seed photons is tied to the blackbody temperature. From the blackbody parameters we derive a blackbody radius, and by accounting for the accretion disk covering factor, we constrain the source distance assuming a 10–12 km NS radius. In § 6 we attempt to obtain information on the geometry of the burning by comparing the persistent and burst spectra. We conclude by summarizing the major results of our work.

TABLE 1
Chandra AND *RXTE* OBSERVATIONS OF GS 1826-238

| Obs. ID | Telescope/ Instrument | Energy Band (keV) | Exp. (ks) |
|------------------------|--------------------------|----------------------|-------------------|
| 2739 | <i>Chandra</i> /ACIS-S | 0.5–8.3 | 68.2 |
| 01,02,000 ^a | <i>RXTE</i> /PCA | 3–23 | 24.6 ^b |
| 01,02,000 ^a | <i>RXTE</i> /HEXTE | 17–200 | 19.4 ^b |

NOTE. — All observations are from 2002 July 29.

^aThe *RXTE* observation IDs are each preceded by 70044-01-01-

^bDue to earth occultation and the satellite's passage through the South Atlantic Anomaly, there are time gaps of 15–30 min in coverage; the times listed represents the sum of 9 separate observation intervals.

2. OBSERVATIONS AND ANALYSIS

In this paper we utilize two simultaneous observations from 2002 July 29, taken with *Chandra* and *Rossi X-Ray Timing Explorer* (*RXTE*). The 68.2 ks *Chandra* observation was made using the Advanced CCD Imaging Spectrometer (ACIS; Garmire et al. 2003) and is sensitive to photons from 0.3–10 keV. The source was focused onto one of the back-illuminated ACIS chips (S3). To minimize the adverse effects due to pile-up, and to gain better time resolution on the rise of the bursts, we used half-frame readout on the inner 4 ACIS chips with 1.74 s frame-time. We use the “level 2” event lists from the standard data processing, and apply a standard correction to destreak the ACIS-S4 chip caused by a flaw in the chip readout. To obtain high resolution spectra, we had the High Energy Transmission Grating (HETG; Canizares et al. 1992) inserted into the optical path.

The 36 ks *RXTE* observation uses the Proportional Counter Array (PCA; Jahoda et al. 1996), and the High Energy X-Ray Timing Experiment (HEXTE; Rothschild et al. 1998). The PCA is made up of five proportional counter units (PCUs) and is sensitive to photons from 2–60 keV. The HEXTE instrument comprises two clusters, each of which contains four NaI/CsI scintillation detectors, and is sensitive to photons from 15–250 keV. Both instruments have large effective areas ($\sim 6000 \text{ cm}^2$ and 1400 cm^2 , respectively) and microsecond timing. Table 1 provides a summary of the GS 1826–238 observations used in the spectral analysis.

2.1. Data Preparation for Spectral Analysis

The *Chandra* HETG Spectrometer is composed of the Medium Energy Grating (MEG) and the High Energy Grating (HEG). The two gratings are slightly offset and appear as “whiskers” traversing all ACIS chips. The MEG is calibrated from 0.3–5.0 keV and the HEG is calibrated from 1.0–8.3 keV. In this analysis, we only made use of the 1st order MEG/HEG data. All of the *Chandra* analysis made extensive use of the Chandra Interactive Analysis of Observations (CIAO) version 3.01 software with calibration version (CALDB) 2.26. We used the CIAO routine *tgextract* for the extraction of grating spectra, *mkgrmf* to produce response matrices, and *fullgarf* to create the auxiliary response matrices. We added the positive and negative diffraction orders and their corresponding auxiliary response files using the script *add_grating_orders*. Systematic errors of 10% were derived from calibration observations of the Crab pulsar and Mrk 421, and were added to both the persistent and burst

emission fits.³ We binned the persistent and burst emission data in the largest possible bins to obtain maximum statistical quality, while maintaining sufficient resolution to observe prominent absorption or emission lines. For the persistent emission analysis we bin the data in 1000 count PHA bins, and in the burst analysis we use 500 count bins. This generally led to bins with width $\sim 50\text{--}100$ eV. We excluded the MEG 1st order data from 0.8–0.9 keV because these data fall on a gap between the ACIS chips. After preliminary analysis, we concluded that the data near 2.1 keV are affected by a residual calibration uncertainty in the response due to an iridium M-edge. To correct for this, we included an inverse edge (e.g., Miller et al. 2002), frozen at 2.065 keV though allowing the optical depth to vary. The best-fit optical depth was consistently ~ -0.16 . In addition, the data from 2.0–2.5 keV are possibly affected by pile-up, which we estimate to be about 10% at the maximum. Spectral distortion due to pile-up is accounted for by the HETG systematics.

The extraction of PCA and HEXTE energy spectra used scripts developed at the University of California, San Diego and the University of Tübingen that incorporate the standard software for *RXTE* data reduction (FTOOLS). The large effective area of the PCA provides excellent statistics without rebinning the data, however the first three channels and the data above 23 keV were not used. We placed systematic uncertainties of 0.5% on the PCA data to account for the likely uncertainty in the response (Kreykenbohm et al. 2004). The HEXTE data below 17 keV and above 200 keV are not included in the analysis. We used successively larger energy bins at higher energies to account for the decreasing flux density. During the burst intervals HEXTE did not yield a significant number of counts above 40 keV. We included no systematics to the HEXTE data. For analysis during the burst time intervals we added the data for the 3 bursts (corresponding to the 2nd, 3rd, and 6th *Chandra* bursts) viewed when PCUs 0 and 2 were taking data; PCUs 0 and 2 had the greatest coverage in this observation. The PHA bins were added together using the FTOOLS task *mathpha*.

3. BURST PERIODICITY AND TIMING CHARACTERISTICS

As discussed in § 1, GS 1826–238 has exhibited a nearly periodic bursting behavior since type I bursts from this source were first discovered in 1997. The remarkable consistency of the burst cycle can easily be seen in Fig. 1. The *Chandra* light curve uses all HETG data from 0.3–8 keV, but does not include any counts from the zeroth order source region as these data are affected by severe pile-up. Not only is the burst recurrence time approximately constant, but the light curve of any particular burst is virtually indistinguishable from any other (see Fig. 1 (c)). Although the time between sequential bursts has been rather constant, the average burst recurrence time has been observed to be steadily decreasing over long time scales (Cocchi et al. 2000, G04). Using a total of 44 *RXTE* observations from 1997 November to 2002 July, G04 measured the burst interval to be 5.74 ± 0.13 hr initially, 4.10 ± 0.08 hr in 2000, and 3.56 ± 0.03 hr in 2002. We measured the average burst recurrence time of the five complete *Chandra* intervals to be 3.54 ± 0.03 hr (12750 ± 102 s; also in 2002). The individual intervals were measured from burst peak to peak and are listed in Table 2. The 2002 recurrence time measurement by G04 was measured using the same PCA data that we use in this paper, while our measurement is based

³ see <http://space.mit.edu/ASC/calib/hetcal.html>

TABLE 2
TIME BETWEEN BURSTS

| Burst Interval | Δt (s) |
|----------------|----------------|
| 1→2 | 12861 |
| 2→3 | 12884 |
| 3→4 | 12510 |
| 4→5 | 12994 |
| 5→6 | 12502 |

NOTE. — The individual burst intervals were measured from the peak of one burst to the next. There is a small uncertainty in these measurements since the *Chandra* data have a frame time (and time resolution) of 1.74 s.

on the *Chandra* data.

The 40% decrease in the burst recurrence time from 1997 to 2002 has been coupled with a 66% increase in the mean persistent flux (G04). Such behavior is expected since the increase in persistent luminosity is assumed to be due to an increase in the global accretion rate, and therefore less time is required to reach the critical amount of fuel. While the observations of G04 are consistent with this trend, Bildsten (2000) found exactly the opposite behavior in many low accretion rate LMXBs. For example, bursts from 4U 1705–44 became less frequent as \dot{M} increased. To explain the conundrum, Bildsten (2000) suggested that a greater fraction of the stellar surface of 4U 1705–44 may be covered prior to ignition, so that the accretion rate per unit area actually decreased. This may also be the case for GS 1826–238: If the relation between the rise in the persistent flux and the decrease in the burst recurrence time were linear, we would expect an even greater decrease in burst recurrence time than has been observed by G04. Another possible explanation for the longer-than-expected recurrence time regards the fact that at smaller recurrence times, less helium will be made prior to ignition, and so the column depth required to produce the instability will increase (Cumming & Bildsten 2000).

The location of the burning during bursts is not assumed to be spherically symmetrical. It is likely that ignition begins near the stellar equator since matter is preferentially deposited there during accretion (Spitkovsky et al. 2002). The anisotropic burning caused by the hot spot at the point of ignition may be revealed through the observation of burst oscillations, the frequencies of which correspond to the NS rotation frequencies (e.g., Muno 2004).

We searched for burst oscillations by computing and averaging the power spectra for the 3 bursts observed with 125 μ s resolution event mode PCA data using a sampling rate of 2048 Hz (Nyquist frequency: 1024 Hz). To improve statistics, we averaged power spectra for sequential 0.25, 0.5 and 1 s sections of the light curve (4, 2, and 1 Hz resolution), with total segment lengths varying from 3 to 30 s. We searched in the ~ 10 s rise, around the burst peak, and at different times during the burst decay until 65 s from the burst peak. PCA deadtime effects cause a $\sim 1\%$ decrease in the mean value of the Poisson noise to 1.98 (from 2.0) in the Leahy normalization (see Leahy et al. 1983). We initially included the entire 2–60 keV energy band and made no significant detections at any point during the burst. We then tried varying

the energy ranges included in the PCA light curves. With the 10–30 keV data, we made a detection 15–30 s from the burst peak around 612 Hz (Figure 2). The significance of the signal was maximized with 0.25 s segment light curves; therefore, 180 separate power spectra were averaged. The signal could be observed in each burst separately though with less significance. We then tried expanding the energy range that was included in the PCA light curves; the signal weakened with the inclusion of either higher and lower energy photons. The 10–1024 Hz Leahy-normalized power spectrum is presented in Figure 2, along with a power spectrum centered on the signal and a histogram of the difference in power from the mean. The power at 612 Hz deviates from the Poisson level by 4.7σ , which with 256 bins means that there is a 0.033% chance that the detection is spurious. Using a power spectrum with 1 Hz resolution, we fit a Lorentzian function to the peak, giving a frequency $\nu_0 \approx 611.2$ Hz with $\Delta\nu_{\text{FWHM}} \approx 3.1$ Hz. The average rms amplitude of the peak is 4.8%, which is consistent with the 5% rms amplitude of typical burst oscillations observed in LMXBs (Muno 2004).

4. PERSISTENT EMISSION SPECTRUM

4.1. Evolution Between Bursts

Along with burst energetics and timing, we can learn much from GS 1826–238 through its energy spectra. We began our investigation by creating spectra for 1 ks intervals following the onset of a burst in order to see if there were significant changes in the best-fit parameters between bursts. Since the average burst recurrence time for the five complete burst intervals in the 68 ks *Chandra* observation was measured to be 12750 ± 102 s, we were able to create 1 ks intervals up to 11–12 ks after the burst. To improve statistics we stacked the datasets from all five *Chandra* burst intervals. We also constructed nearly two complete burst intervals using the simultaneously acquired *RXTE* data. Although these data have time gaps, we determined the time since the previous burst for any individual *RXTE* dataset by comparing it to the *Chandra* burst times. With the benefit of the simultaneous observations we obtained statistically significant measurements from 0.5–200 keV for each 1 ks interval (except 9–10 ks). To each dataset, we fit a model composed of Comptonized emission plus a broken power law. This preliminary model was only used to examine whether or not there were significant changes to the spectrum with time, and ultimately, a different model was determined to be more physically plausible (see below). Nevertheless, this exercise showed us that the best-fit parameters remain approximately constant after 1 ks, although with slightly elevated soft X-ray flux through 3 ks from the peak of the burst. In the following fits, we therefore define the persistent spectrum to be for $t > 3$ ks. In the integrated persistent emission analysis below, we found that the inclusion of data from 1–3 ks only minimally distorted most spectral parameters, however the inferred N_{H} was underestimated by $\sim 50\%$ due to the excess of soft photons.

We are fortunate to have *Chandra* data along with *RXTE* since observations of bursters with low-Earth orbit telescopes may miss some bursts if they occur during a gap in coverage when the source is occulted by the Earth or the telescope is passing through the South Atlantic Anomaly. Fig. 1 (b) provides an illustration of the potential ambiguity involved with the selection of persistent emission datasets. For example, it is clear that any persistent emission analysis would be slightly distorted if the first 3 ks of the second PCA observation (corresponding to the decay of the first burst observed

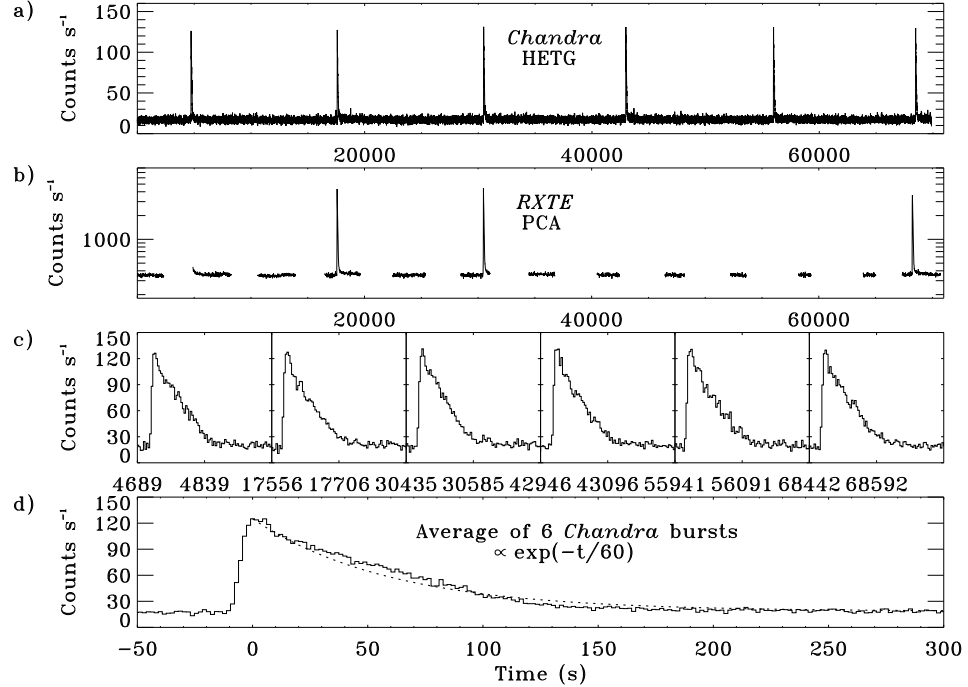


FIG. 1.— Light curves for the *Chandra* HETG and *RXTE* PCA instruments. The top two light curves (*a* and *b*) show the intervals when each telescope was taking data. The *Chandra* light curve includes the HETG data from 0.3–8 keV and has time resolution of 3.48 s, as does the data in plot (*c*). The PCA light curve includes data from 3–8 keV and uses 16 s time bins. The time axis of the top three plots begins at MJD 52484.2039. The lower plots show the individual (*c*) and average (*d*) of the 6 *Chandra* bursts. We used the smallest possible binning of 1.74 s, and the curves were aligned using the rises of the bursts. The zero point reference time for plot (*d*) also corresponds to the peak of the burst. The curve can be approximated by a decaying exponential with scale time 60 s, however this value cannot be interpreted physically since it includes all instrumental effects resulting from differences in the detector response with energy.

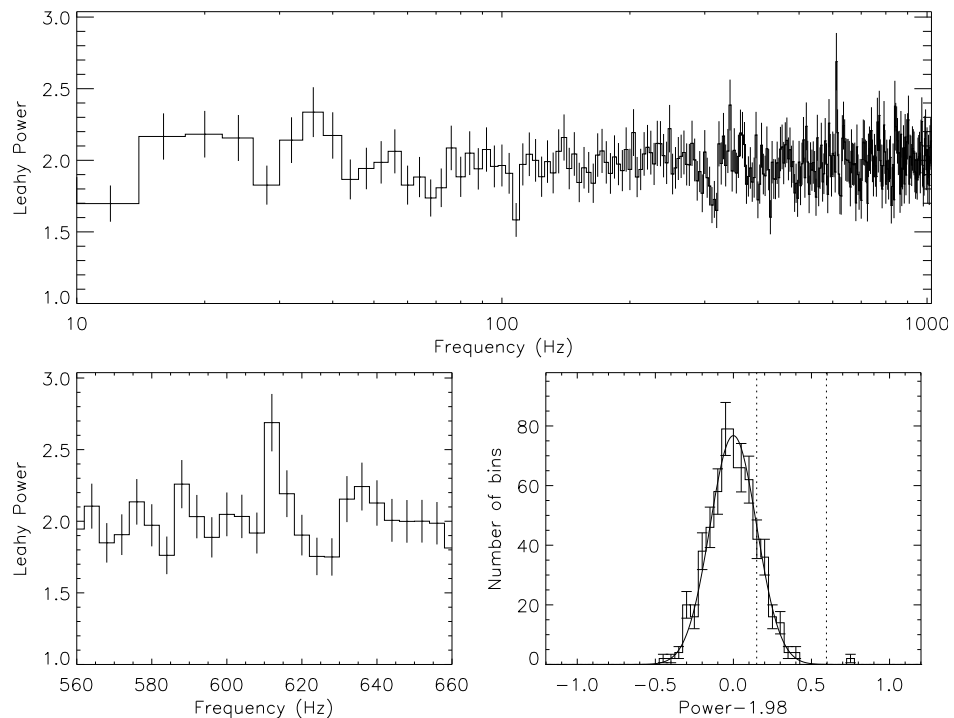


FIG. 2.— Averaged Leahy-normalized power spectrum for the 3 bursts (15–30 s from burst peak) observed with PCA (top and bottom left), and a histogram of the distribution of the powers scaled to zero mean (bottom right). The frequency bins are 4 Hz. The vertical dashed lines in the bottom right sub-figure represent 1σ and 4σ standard deviations from the mean. The power at 611.2 Hz deviates from the Poisson level by 4.7σ .

with *Chandra*) were included.

4.2. Integrated Spectrum

By summing all PHA datasets that fall within the 3–12 ks interval, we further constrain the statistics and explore standard models for LMXBs in addition to other models. LMXBs are typically modeled with a blackbody or disk blackbody to represent the NS surface or the inner accretion disk, plus Comptonized emission which can be modeled in XSPEC with `comptt` or a cut-off power law (`cutoffpl`). Although these models have similar profiles, they are not necessarily interchangeable. While Comptonized emission can be empirically described with a cut-off power law, the model of Titarchuk (1994) is derived from analytical equations that are founded on the real analytical theory of Comptonization of soft photons, and the output parameters are physically explicit which allow direct interpretation. On the contrary, the index of a cut-off power law cannot be interpreted in physical terms, while in `comptt` it is related to the combination of the optical depth and plasma temperature. Albeit, the cut-off energy of `cutoffpl` is related to the plasma temperature as $E_{\text{cut}} \sim 2kT_e$. For these reasons we chose the Titarchuk (1994) model to represent Comptonized emission. With this description, the spectrum is governed entirely by the plasma temperature and the β parameter, which characterizes the distribution law of the number of scatterings (i.e., $P(n) \propto \exp(-\beta n)$) is the probability that a seed photon undergoes n scatterings before escaping the plasma). The optical depth of the plasma is calculated from the β parameter and depends on the input geometry: disk or spherical. Generally, for a given β parameter, a larger optical depth is inferred from a spherical geometry than a disk geometry. This is because the final spectral shape is determined by photons which undergo many more scatterings than the mean, and the longest dimension of a spherical plasma cloud is clearly shorter than that of a disk (Titarchuk 1994).

We initially tried to fit the data by employing a single `comptt` component, but the resulting fit was unacceptable due to excesses above 70 keV and below 1.5 keV. The addition of a blackbody component reduced the soft excess, and allowed the plasma temperature and thus the up-scattering efficiency to increase (since $\langle E_f \rangle \sim \langle E_i \rangle e^\gamma$, where $\gamma \equiv 4kT_e\tau^2/m_ec^2$ is the Comptonization parameter) to try to match the hard excess. Although the fit was better ($\chi_\nu^2 = 1.30$), it was still unacceptable. This is contrary to the results of in 't Zand et al. (1999a), who successfully used this model, although the 3.8 keV best-fit blackbody temperature is probably non-physical. The best-fit blackbody temperature that we obtained with this model was ~ 0.5 keV, which seems more reasonable.

After trying various models in conjunction with `comptt`, we found the fit to be most improved by an additional `comptt` component, resulting in a model that can be interpreted as the Comptonization of soft photons from two distinct emission regions. One of the emission regions contributes 62% of the total luminosity, so we label it as the “primary” emission region, and the other as the “secondary” emission region. The primary emission region is characterized by $kT_s \sim 0.3$ keV, and $kT_e \sim 19.7\text{--}22.1$ keV (depending on the chosen geometry), while the secondary emission region has $kT_s \sim 0.8$ keV and $kT_e \sim 6.1\text{--}6.4$ keV. The primary emission accounts for about 70% of the flux from 0.5–3 keV, and 80% of the flux from 20–200 keV, while each Comptonization component contributes nearly an equal amount of flux for 3–

20 keV. Based on the inferred β parameter, which is not a direct input in XSPEC, the primary emission region has $\tau \sim 2.7$ if the region is disk-shaped, or $\tau \sim 6.3$ if it is spherical. The secondary emission region is characterized by $\tau \sim 4.7$ and $\tau \sim 9.9$ for disk and spherical geometries, respectively.

The physical interpretation of each Comptonizing region must be inferred from the best-fit parameters and the corresponding flux contributions. For one, we expect the Comptonizing region closer to the stellar surface to have hotter seed photons, which suggests that the secondary component is emitted nearer to the NS. The secondary component may therefore result from boundary layer or surface emission. Conversely, the primary emission possibly stems from the accretion disk or ADC, and a disk geometry implies $\tau \sim 2.7$. From the relative flux contributions, we see that this interpretation requires about 3/5 of the total flux to be emitted from the cooler disk region. Accretion theory predicts that half of the total gravitational binding energy per unit mass is released in the disk, and the other half in the boundary layer or on the stellar surface (Frank et al. 1985). This is not inconsistent since the accretion disk and the boundary layer are not physically distinct; rather, there may be a smooth transition from one to the other. Secondly, the optical depth of the secondary emission (independent of the true geometry) is large enough to naturally explain the lack of a visible blackbody component in the GS 1826–238 spectrum. According to Inogamov & Sunyaev (1999), the spreading of accretion flow from the equator to the poles leads to two bright rings of enhanced emission that are symmetric about the equator. The latitude of these rings increases with accretion rate, and in the accretion regime of GS 1826–238, i.e. $\sim 10^{17}$ g s⁻¹ (inferred from the total flux), these rings lie $\sim 0.5\text{--}1.5$ km from the equator. Therefore, assuming the blackbody emission comes from these rings, the secondary Comptonized emission region only has to be large enough to cover the inner ± 1.5 km above and below the equator. Following in 't Zand et al. (1999b), an approximate effective radius for the spherical emission area of the Wien seed photons is given by $3 \times 10^4 d \sqrt{\frac{F_{\text{cut}}}{1+y}} / (kT_s)^2$ km, where d is in kpc, the flux is measured in erg s⁻¹ cm⁻², and the seed photons are measured in keV. This approach yielded a soft photon emitting region with radius $R_s \sim 4d_{\text{kpc}}$ km, which is only consistent with the seed photons being generated at the boundary layer if the region is confined to a half-thickness of ~ 2.5 km, depending on the inclination of the system, and assuming that any emission from “below” the accretion disk is not observable. Finally, since the flux of photons passing through the boundary layer relative to the disk is larger per unit area, we expect Compton cooling to maintain a lower plasma temperature for the secondary Comptonized emission region. This is indeed what is observed (see Table 3).

In addition to a dual Comptonization model, we also modeled the spectrum with a single `comptt` plus a broken power law in order to give an estimate of its shape for possible non-thermal interpretation. If the secondary emission is indeed non-thermal, perhaps it stems from an ADC generated by magnetohydrodynamic turbulence, analogous to what is observed in the solar corona (Crosby et al. 1998). Alternatively, the emission may be synchrotron radiation from a relativistic jet escaping the system. Such jets have been found to be rather common among LMXBs and link these systems to active galactic nuclei (AGNs) (e.g., Fender 2002). Clearly, these possibilities are highly speculative.

4.3. Iron Line Detection

After obtaining a fit with the two component models, the residuals revealed a line feature around 6.5 keV, which prompted the addition of a Gaussian to the models. The best-fit value for the line was measured to be approximately 6.45 keV, with a flux which corresponds to an equivalent width (EW) of ~ 37.2 eV. We interpret this feature as a neutral Fe K α line. An F-test showed that the probability for an improvement to the fit occurring by chance is 5.3×10^{-5} for the dual Comptonization model, and 6.8×10^{-4} for the Comptonization plus broken power law model. However, it should be noted that the use of an F-test to measure the significance of lines may not be valid (Protassov et al. 2002). We present the best-fit parameters for these models in Table 3. We also present the results of a blackbody plus cut-off power law model, which is described below. To account for the uncertainties in the relative instrumental flux calibrations, we introduced a multiplicative constant into the spectral models. For each model, the normalizations of the *Chandra* instruments relative to PCA were ~ 0.95 , while for HEXTE the relative normalization was generally $\sim 0.85\text{--}0.9$. Figure 3 shows the spectral fit for the dual Comptonization model, and the residuals for all three models.

4.4. Comparison to Previous Fits

To facilitate comparison to the results of previous work, we also fitted the spectrum of GS 1826–238 with a blackbody plus cut-off power law model (model 3), and a blackbody plus power law from 0.5–10 keV (not included in the table). These models have been used by others to provide acceptable fits to the GS 1826–238 persistent emission, but only the *BeppoSAX* observations had similar energy coverage. For example, the ASCA SIS instrument used in the Kong et al. (2000) analysis did not provide coverage above 10 keV, and the Barret et al. (1995) *ROSAT* observation was restricted to energies below 2.2 keV. In order to compare to the Kong et al. (2000) results, we used the same blackbody plus power law model and omitted all data above 10 keV. With this approach we obtained a fit with $kT_{bb} \sim 0.8$ keV and $\Gamma \sim 1.0$, which are each within $\sim 15\%$ of their results. Extending the energy range to 200 keV, however, revealed a higher blackbody temperature, a steeper photon index, and the power law had to be changed to a cut-off power law (model 3). This shows that the use of *RXTE*'s extended energy range is crucial to minimize uncertainties in the soft component parameters due to less precise knowledge of the photon index or Comptonized component when measured with the lower *Chandra* energy range.

As mentioned in §§ 1 and 4.2, in 't Zand et al. (1999a) fit the 0.1–200 keV persistent emission spectrum with a blackbody plus *comptt*, but they also modeled the spectrum with a blackbody plus a cut-off power law. The best-fit blackbody temperature was ~ 0.9 keV, $\Gamma \sim 1.4$, $E_{cut} \sim 52$ keV, and $N_H \sim 5.4 \times 10^{21} \text{ cm}^{-2}$, which slightly differs from $kT_{bb} \sim 1.3$ keV, $\Gamma \sim 1.3$, $E_{cut} \sim 42$ keV, and $N_H \sim 4.3 \times 10^{21} \text{ cm}^{-2}$ of model 3. If we set the model 3 parameters to those obtained by in 't Zand et al. (1999a), however, we obtain a similar $\chi^2_\nu \sim 1.4$.

By examining the residuals, the slope of the model 3 appears to be too steep from $\sim 2.5\text{--}5$ keV and 12–20 keV, and too shallow for $\sim 5\text{--}12$ keV. A slight excess also remains for energies above about 60 keV (see Fig. 3 bottom). The 2.4 km blackbody radius derived from this model is obviously smaller than expected for a NS, though the size of the radius may be

explained if the blackbody emission is confined to the equatorial region. For a 10 km NS, a blackbody radius of 2.4 km would correspond to emission from a strip of half-height ~ 0.6 km. We note that since $E_{cut} \sim 2kT_e$, the ~ 42 keV cut-off energy is consistent with the ~ 20 keV plasma temperature of the primary Comptonized component of model 1. However, unlike the dual Comptonization model and the Comptonized emission plus broken power law model, the addition of a line feature at ~ 6.45 keV to model 3 did not significantly improve the fit, though we include it to preserve consistency. We place an upper limit on the equivalent width at 15.2 eV with 90% confidence.

Even though the blackbody plus cut-off power law fit that we obtained is acceptable, we are less confident with this model as compared to model 1 since the inferred N_H is inconsistent with the value obtained through the galactic hydrogen survey of Dickey & Lockman (1990), where the average column density in the direction of GS 1826–238 was found to be $\sim 1.9 \times 10^{21} \text{ cm}^{-2}$. Moreover, such a high column density is inconsistent with the X-ray halo measurements presented by Thompson et al. (2005, in preparation). Briefly, for the X-ray halo analysis we created an exposure-corrected radial profile of the source and subtracted a normalized model point spread function to obtain the X-ray halo profile. Using empirical relations from the dust scattering analysis of Draine (2003), we found that $\lesssim 3\%$ of the source flux is scattered into the X-ray halo. This result was then used to obtain a scattering optical depth, which can be converted to an approximate hydrogen column density through a linear regression derived using observations of X-ray halos around 29 sources (cf. Predehl & Schmitt 1995, Fig. 7). The hydrogen column density that we obtained in this fashion is consistent with the best-fit value of models 1 and 2. By freezing N_H in model 3 to the common lower value, the model fits the data poorly. We therefore conclude that the common LMXB model of a blackbody plus Comptonized emission described by *comptt* or *cutoffpl* is not appropriate for the persistent emission spectrum of GS 1826–238.

4.5. Interstellar Absorption Features

The persistent emission spectrum was searched for interstellar absorption features. This effort turned up a good candidate at about 17.15 Å. The feature is broad (0.102 ± 0.027 Å FWHM) with an optical depth at line center of 0.63 ± 0.09 , when fitted with a Gaussian. The formal significance is about 3.8σ ; based on about 800 bins searched at 0.03 Å binning, there is about a 6% chance that one would find such a feature due to random fluctuations. Including a narrower feature at about 17.5 Å with a significance of 2.9σ , we modeled both features with structure in the Fe L edge due to the interstellar medium (ISM). The wavelengths of these features are a good match to those of Fe L III at 17.51 Å and Fe L II at 17.19 Å. The match is not perfect. Figure 4 shows the near edge extended absorption fine structure (NEXAFS) of the Fe L edge as measured by Kortright and Kim (2000) and the edge structure of butadiene iron tricarbonyl ($C_7FeH_6O_3$) from the Corex data base maintained by A. P. Hitchcock⁴. Neither model matches the data without a slight energy shift to match the L III feature. Furthermore, the 17.15 Å line is somewhat broader than expected and may have an excess of absorption at the short wavelength side. Schulz et al. (2002) identified

⁴ see <http://unicorn.mcmaster.ca/corex>

TABLE 3
PERSISTENT EMISSION SPECTRAL PARAMETERS

| Model: | 1. Two Comptonized (disk + spherical) ^a | 2. Comptonized plus Bkn. PL ^b | 3. Blackbody plus CPL ^c |
|--|---|--|---------------------------------------|
| $N_H (\times 10^{21} \text{ cm}^{-2})$ | $1.60^{+0.33}_{-0.61}$ | $1.50^{+0.06}_{-0.06}$ | $4.29^{+0.21}_{-0.19}$ |
| $kT_d/kT_s _{\text{seed}}, kT_{\text{bb}}^d$ (keV) | $0.42^{+0.05}_{-0.03}/0.82^{+0.05}_{-0.03}$ | $0.68^{+0.01}_{-0.01}/0.86^{+0.04}_{-0.03}$ | $1.34^{+0.04}_{-0.04}$ |
| R_s, R_{bb}^e (km) | $4.02^{+0.54}_{-0.37}$ | $5.88^{+0.43}_{-0.39}$ | $2.38^{+0.19}_{-0.18}$ |
| kT_d/kT_s electron (keV) | $20.79^{+0.72}_{-1.08}/6.84^{+0.38}_{-0.33}$ | $5.85^{+0.28}_{-0.19}/4.74^{+0.32}_{-0.22}$ | ... |
| τ_d/τ_s | $2.56^{+0.04}_{-0.04}/9.38^{+0.04}_{-0.04}$ | $4.69^{+0.03}_{-0.04}/10.98^{+0.23}_{-0.18}$ | ... |
| y_d/y_s | $1.07^{+0.07}_{-0.09}/4.71^{+0.30}_{-0.27}$ | $1.01^{+0.06}_{-0.05}/4.47^{+0.49}_{-0.35}$ | ... |
| Γ_1^f | ... | $1.19^{+0.01}_{-0.03}$ | $1.26^{+0.01}_{-0.02}$ |
| Γ_2 | ... | $2.43^{+0.05}_{-0.04}$ | ... |
| $E_{\text{break}}, E_{\text{cut}}$ (keV) | ... | $35.41^{+0.52}_{-0.47}$ | $41.58^{+1.49}_{-1.60}$ |
| E_{line} (keV) | $6.44^{+0.03}_{-0.12}$ | $6.45^{+0.02}_{-0.10}$ | $6.37^{+0.12}_{-0.11}$ |
| EW_{line} (eV) | $37.2^{+10.1}_{-8.4}$ | $28.3^{+4.3}_{-11.9}$ | 15.2^g |
| χ_{ν}^2 (d.o.f.) | 0.70 (521) | 0.75 (522) | 0.84 (527) |

NOTE. — All errors are quoted at the 90% confidence level for a single parameter.

^aXSPEC: phabs*edge(comptt + comptt + gauss)

^bXSPEC: phabs*edge(comptt + bknpower + gauss)

^cXSPEC: phabs*edge(bbbody + cutoffpl + gauss)

^dThe parameters for spherical and disk geometries are listed as “disk/spherical”, or “primary/secondary” for models 1 and 2. The two geometries are fit together in model 1, and separately in model 2.

^eThe spherical Wien emission radius and the blackbody radius. The derivation of the Wien radius is described in § 4.2. The blackbody radius is defined by the relation $L_{\text{bb}} = 4\pi R_{\text{bb}}^2 \sigma T_{\text{eff}}^4$, where σ is the Stefan-Boltzmann constant. The blackbody normalization in XSPEC is defined to be L_{39}/D_{10}^2 , where L_{39} is the blackbody luminosity in units of 10^{39} erg s⁻¹ and D_{10} is the distance to the source in units of 10 kpc. The derivation R_{bb} uses a ratio $T_{\text{bb}}/T_{\text{eff}} = 1.4$ (Ebisuzaki et al. 1984, also see § 5), and a source distance of 6 kpc.

^fThe model 2 broken power law parameters are independent of the geometry of the Comptonizing region.

^gThis equivalent width is an upper limit.

the Fe L features in the spectrum of Cyg X-1 and suspected that there is a mix of Fe molecules, citing, in particular, a feature near 17.15 Å that might be due to a more pure form of Fe. Without the corresponding L III feature in our spectrum, however, we suspect that the extra broadening might result from statistical fluctuation. The models use a cosmic abundance of Fe (4×10^{-5} relative to H) and the observed ISM column density of $2.0 \times 10^{21} \text{ cm}^{-2}$. Thus, these absorption features are consistent with Fe in the ISM.

5. BURST SPECTRUM AND EVOLUTION

We also studied the evolution of the spectrum throughout the burst and its decay by subdividing the first 1 ks from burst peak into 8 datasets with progressively larger integration times (Table 4). Those data above 40 keV were ignored as too few counts were obtained for significance. All of the datasets were fit with the XSPEC model phabs*edge(comptt_d + comptt_s + bbbody) (d: disk, s: sphere), with the hydrogen column density frozen at the common value of $1.85 \times 10^{21} \text{ cm}^{-2}$. We initially allowed the disk Comptonization parameters to vary, but the best-fit values for each dataset, including the normalizations, changed by $\lesssim 5\%$, so they were frozen at the persistent emission values. Since the blackbody emission during a burst provides a large influx of seed photons in the inner boundary layer, the spherical seed photon temperature was fixed to the blackbody temperature, which is justified since most Comptonized emission is emitted within ~ 20 km of the surface of the NS (Frank et al. 1985). Table 1 shows the evolution of the spectral parameters.

Using the results from Table 4, we can place an upper limit to the source distance assuming the blackbody luminosity is

Eddington-limited, which it is not since the bursts are significantly sub-Eddington. During the first 10 s following the peak of the burst, the average flux from 0.5–40.0 keV was measured to be $1.96 \times 10^{-8} \text{ erg cm}^{-2} \text{ s}^{-1}$. We corrected the peak flux by assuming an approximately constant spectrum for this interval (i.e. constant spectral parameters), and by measuring the burst decay scale time (~ 35 s over the energy band). The peak flux was found to be $\sim 12\%$ larger than the 0–10 s mean, or $2.2 \times 10^{-8} \text{ erg cm}^{-2} \text{ s}^{-1}$. Moreover, we must account for radiation that is absorbed or scattered out of the line-of-sight on its way to the telescope. The hydrogen column density toward the source was assumed to be about $2 \times 10^{21} \text{ cm}^{-2}$, which corresponds to a scattering optical depth of 0.02 (Predehl & Schmitt 1995). Thus scattering and absorption along the line of sight reduce the observed flux by $(1 - e^{-0.02}) \approx 0.02$. If we assume that the blackbody normalization is also $\sim 12\%$ larger than the 0–10 s mean, and that the *unabsorbed* normalization is $\sim 2\%$ larger still, we arrive at a maximum source distance of 9.2 kpc⁵ for the bursts being at the Eddington limit. This upper limit on the distance is consistent with the 8 kpc upper limit derived by in ’t Zand et al. (1999a).

The thermal nature of the burst spectrum with a blackbody temperature of ~ 1.8 keV, accompanied by the cooling, is typical for a type I X-ray burst (Lewin et al. 1995). While the blackbody temperature decreases by a factor of about 2.2 dur-

⁵ In this derivation we do not include the flux contributions from radiation that is thought to be emitted from outside the NS surface, since this radiation would not provide an impediment to the accretion rate. Therefore, we do not include the Comptonized emission. (This interpretation is clearly debatable.) The blackbody normalization is defined in Table 3 comment *e*. We also assume a $1.4 M_{\odot}$ NS.

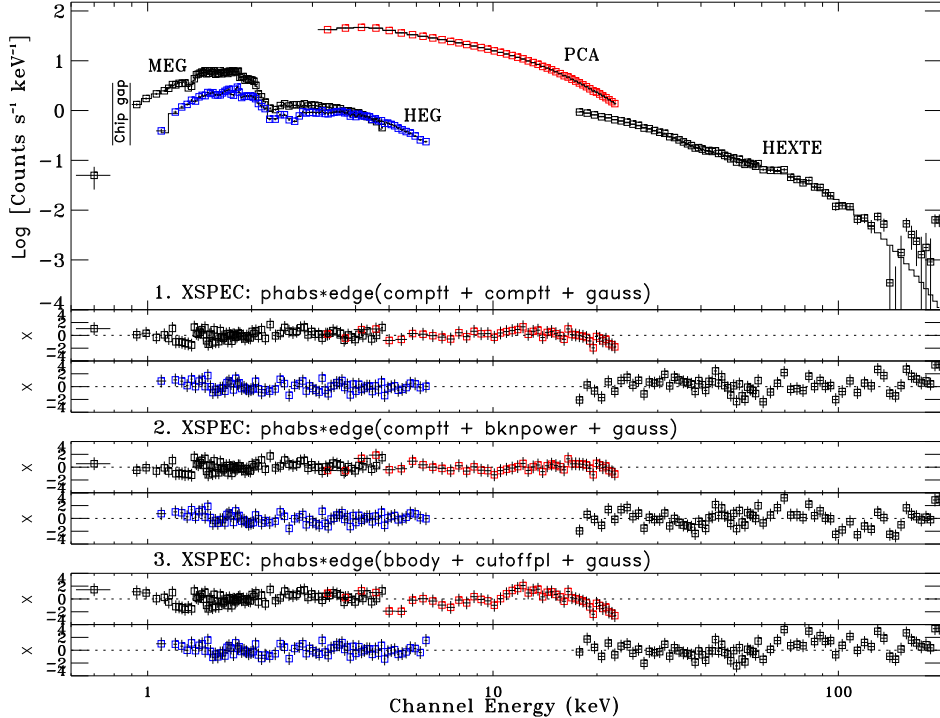


FIG. 3.— Persistent emission spectrum and residuals of the dual Comptonization model (1), and the residuals of models 2 and 3. For each model, the upper residuals are for the MEG and PCA, and the lower residuals are for the HEG and HEXTE. The range 0.8–0.9 keV is ignored since these MEG counts fall on a gap between ACIS CCDs. To provide clarity, we have only plotted every third (second) MEG (HEG)

TABLE 4
SPECTRAL EVOLUTION DURING BURST DECAY

| Interval ^a (s) | kT _{bb} (keV) | Norm. ($\times 10^{-2}$) | R _{bb} (km) | kT _e (keV) | τ | F _X : 0.5–10.0 keV ($\times 10^{-9}$ erg s ⁻¹ cm ⁻²) | 0.5–40.0 keV |
|------------------------------|--|--------------------------------------|--------------------------------------|-------------------------------------|--------------------------------------|--|--------------|
| 0–10 | 1.76 ^{+0.06} _{-0.04} | 12.0 ^{+0.6} _{-1.5} | 11.6 ^{+0.8} _{-1.6} | 3.1 ^{+0.6} _{-0.2} | 9.9 ^{+22.1} _{-5.7} | 13.5 | 19.6 |
| 10–30 | 1.72 ^{+0.04} _{-0.03} | 10.8 ^{+0.5} _{-0.5} | 11.5 ^{+0.5} _{-1.2} | 3.8 ^{+0.6} _{-0.3} | 7.8 ^{+3.7} _{-3.8} | 10.4 | 14.9 |
| 30–65 | 1.50 ^{+0.08} _{-0.08} | 5.1 ^{+0.2} _{-0.2} | 10.4 ^{+1.3} _{-1.1} | 4.3 ^{+0.3} _{-0.5} | 8.0 ^{+18.6} _{-5.2} | 7.1 | 10.4 |
| 65–100 | 1.24 ^{+0.11} _{-0.11} | 3.1 ^{+1.3} _{-1.9} | 11.9 ^{+3.3} _{-2.8} | 4.5 ^{+0.9} _{-0.7} | 10.2 ^{+5.6} _{-4.1} | 3.8 | 6.6 |
| 100–150 | 1.01 ^{+0.19} _{-0.19} | 0.6 ^{+0.7} _{-0.6} | 7.9 ^{+5.5} _{-4.6} | 5.0 ^{+1.4} _{-0.9} | 11.8 ^{+6.2} _{-4.4} | 2.0 | 3.6 |
| 150–200 | 0.86 ^{+0.08} _{-0.06} | ... | ... | 7.1 ^{+0.9} _{-2.2} | 11.2 ^{+5.5} _{-0.7} | 1.4 | 2.9 |
| 200–500 | 0.83 ^{+0.05} _{-0.05} | ... | ... | 6.8 ^{+1.4} _{-1.6} | 8.7 ^{+1.1} _{-0.9} | 1.4 | 2.9 |
| 500–1000 | 0.81 ^{+0.06} _{-0.03} | ... | ... | 6.9 ^{+0.6} _{-0.4} | 9.2 ^{+0.6} _{-0.3} | 1.3 | 2.8 |

NOTE. — All errors are quoted at the 90% confidence level for a single parameter. The XSPEC model used in this analysis was phabs*edge(comptt_d + comptt_s + bbody). Only the last two components had free parameters. The column density was set to $1.85 \times 10^{21} \text{ cm}^{-2}$, and the parameters describing disk Comptonization were fixed to the persistent emission best-fit values. The seed photon temperature of the spherical Comptonizing region was tied to the blackbody temperature. Good fits were obtained with χ^2_{ν} consistently ~ 0.9 .

^aThe peak of the burst is defined to take place at $t = 0$.

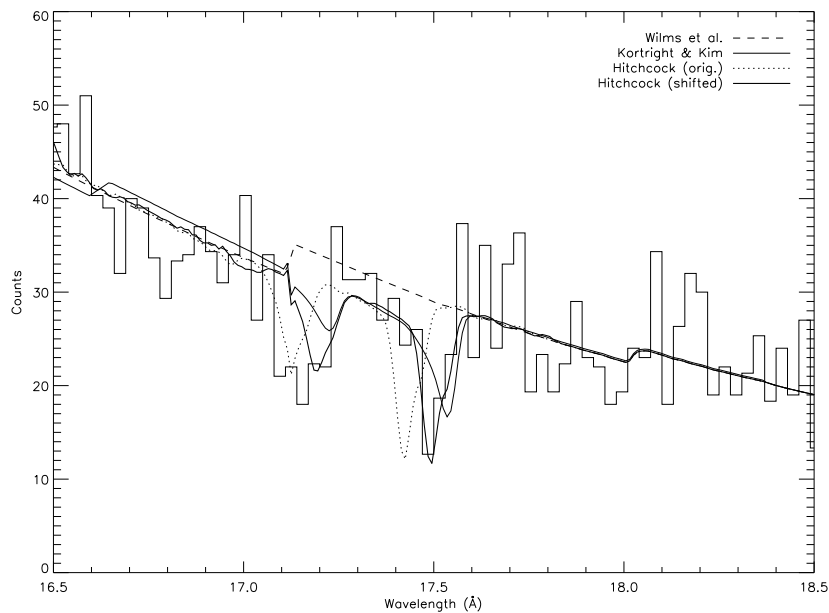


FIG. 4.—Spectrum of the persistent emission of GS 1826–238 near 17.5 Å. A global model of the continuum is shown for several models of the Fe L edge complex due to the ISM. *Dashed curve*: The ISM opacity model provided in the `tbabs` model of XSPEC, using the prescription provided by Wilms et al. (2000). *Thin curve*: The Fe L edge opacity model based on measurements by Kortright & Kim (2000). *Dotted curve*: The Fe L edge structure is based on the transmission of butadiene iron tricarbonyl ($C_7FeH_6O_3$) from the Corex data base maintained by A. P. Hitchcock. *Thick curve*: The model based on the Hitchcock data but shifted by 3 eV to match the data better. The 17.15 Å line is somewhat broader than expected and may have an excess of absorption at the short wavelength side but these absorption features are generally consistent with a cosmic abundance of Fe.

ing burst decay, the normalization decreases by more than a factor of 30. Nevertheless, the derived blackbody radius remains approximately constant as long as blackbody emission is observable. Figure 5 shows the derived blackbody radius and the fraction of blackbody flux ($F_{\text{bb}}/F_{\text{total}}$) from 2–10 keV during the first 150 s after burst ignition. Clearly these data are consistent with a blackbody radius of ~ 10.3 – 11.7 km, assuming a source distance of 6 kpc and a ratio $T_{\text{bb}}/T_{\text{eff}}$ (spectral hardening factor) of 1.4. Such a correction must be applied since NSs do not radiate as perfect blackbodies during X-ray bursts because the thermalization of photons occurs at scattering optical depths greater than unity, where the temperature is higher than the effective temperature. Rather, the photons are thermalized at optical depths of ~ 4 – 5 (e.g., Ebisuzaki et al. 1984, London et al. 1986, Madej et al. 2004). Assuming that the entire stellar surface is involved when blackbody emission is observable, i.e. the burning does not cease in one area sooner than another, the slight decrease in the inferred blackbody radius for the 100–150 s interval (see Fig. 5) could be explained by a $\sim 10\%$ increase in the spectral hardening factor. This is a possibility since at lower effective temperatures ($T_{\text{eff}} < 1.5$ keV) the spectral hardening factor increases with decreasing temperature, as the relative contribution of electron scattering to the total opacity decreases (London et al. 1986). However, within the error limits, the blackbody radius for this interval is still consistent with the measured values during the first 100 s of the burst.

The derived blackbody radius cannot be interpreted as the physical size of the NS since LMXBs do not have isotropic radiation fields. Due to the presence of an optically thick accretion disk, any blackbody emission from the surface of the NS that is in the “shadow” of the accretion disk would not be directly observed but would possibly emerge as Comptonized emission. The only geometrical arrangement for which we can naively interpret the blackbody radius as the stellar radius is when the accretion disk is perpendicular to the line of sight ($i = 0^\circ$). In all other cases the inferred blackbody radii underestimate the stellar radius, and so one must account for the covered region in order to extract a stellar radius from a measured blackbody temperature and flux.

The area of the covered region increases nonlinearly with increasing binary inclination, moving from 0% of the projected area when $i = 0^\circ$ to 50% when $i = 90^\circ$. Furthermore, since accretion disks are not infinitely thin there will also be some portion of the surface covered by the disk. The amount of covering by the disk can be parametrized by the disk half-height h . In spite of the nonlinear relation between the amount of covering and the inclination and disk half-height, the fraction of the stellar surface that is covered can be calculated using straightforward geometrical principles. With these issues in mind we interpreted πR_{bb}^2 as the observable *projected* area of the star, and by calculating the fraction of surface covered we derived an effective stellar radius (R_{eff}) as a function of inclination and disk half-height for source distances of 6 kpc and 5 kpc, which is presented in Fig. 6. Using optical observations of the counterpart of GS 1826–238, Mescheryakov et al. (2004) were able to derive an approximate inclination of $i \sim 40^\circ$ – 70° , and so we only include this range in the figure.

From photometric measurements of the optical counterpart, Barret et al. (1995) derived an approximate lower limit to the distance to GS 1826–238 of 4 kpc. Assuming the range of possible binary inclinations used above is correct, it is apparent that a source distance near 5 kpc gives a NS radius within the commonly assumed range of ~ 10 – 12 km (see the right

axis of Fig. 6). On the contrary, a distance of 6 kpc does not give a NS radius within the common range. Even with an infinitely thin accretion disk and an inclination at the lower bound ($i = 40^\circ$) of Mescheryakov et al. (2004), the smallest possible stellar radius at this distance within the error limits is ~ 11 km.

From the results of the Table 4, it is clear that the burst photons immediately cool the Comptonizing plasma to ~ 3.4 keV. Over the next 150 s, the plasma temperature recovers the persistent emission value of ~ 6.8 keV. This type of plasma cooling during a burst may be an example of Compton cooling. The same inverse Compton scattering process that transfers energy to the persistent emission photons also transfers energy to the photons emitted during a burst. The difference is that during the burst the flux of photons increases by more than an order of magnitude (for the 0–10 s interval), so that the balance between heating and radiative cooling is disturbed. It is also evident that the optical depth of the plasma is weakly constrained in the burst spectral analysis. Although the best-fit values for the first few intervals seem to indicate a larger optical depth, the range of uncertainty still includes the persistent emission value.

6. EMISSION REGION GEOMETRIES

Since blackbody emission is observable during the bursts but not during the quiescent phase, we can speculate as to the geometries of the corresponding emission regions. To begin, GS 1826–238 has a weak magnetic field so infalling matter probably impacts the NS along the equator rather than at the poles. The release of gravitational binding energy through thermalization of the accreted material may result in a strip of blackbody emission along the equator (Church & Bałucińska-Church 2001), or the accumulation and spreading of accretion flow from the equator toward the poles may cause two bright emission rings that are symmetric about the equator (Inogamov & Sunyaev 1999). The inability to see blackbody emission in the interval between bursts suggests that the equatorial strip or enhanced bright rings must be covered by an optically thick layer. This is explained naturally by the persistent emission dual Comptonization model.

At the onset of a burst, ignition likely starts near the equator and then rapidly spreads to cover the entire stellar surface in a couple seconds or less (Spitkovsky et al. 2002). Once the entire accumulated layer is burning, the subsequent blackbody emission indicates that there is an optical path for the radiation outside of the equatorial strip. It could be argued that the accretion flow is disrupted during a burst, or that a spherical corona surrounding the NS is temporarily blown away, and that this provides a path for the blackbody emission. However, the flux provided by the inner Comptonizing region also increases substantially during a burst, so the boundary layer plasma must still be present to up-scatter the seed photons. Moreover, our measurement of the Wien emission radius (~ 4 km) is too small for the corona to completely surround the star. Instead, we assume that this emission region is likely confined to the equatorial region. This explanation supports theories where the Comptonizing plasma or ADC is geometrically thin.

7. SUMMARY

Our investigation of the LMXB GS 1826–238 using simultaneous *RXTE* and *Chandra* observations has led us to the following conclusions. From the observation of five uninterrupted burst intervals with *Chandra* in July 2002, we mea-

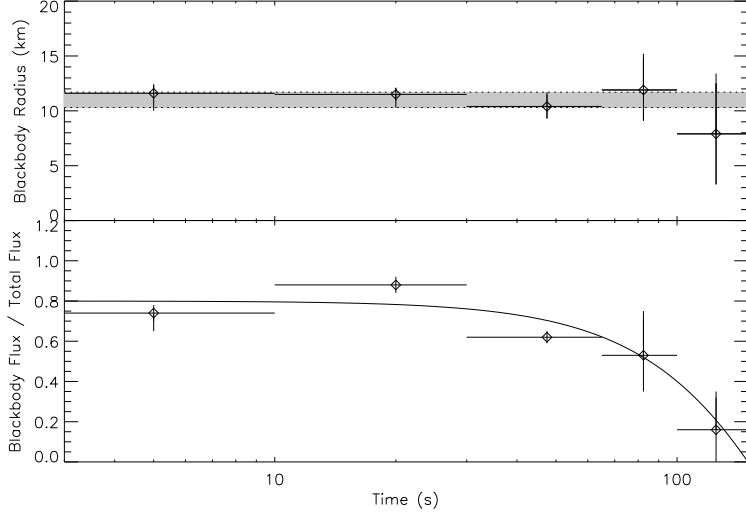


FIG. 5.— Blackbody radius and fraction of blackbody flux ($F_{\text{bb}}/F_{\text{total}}$) from 2–10 keV during the first 150 s after burst ignition. The bottom curve is fit “by eye” with a cosine. Beyond 150 s, the XSPEC blackbody normalization decays to zero. These data are consistent with a blackbody radius between 10.3 and 11.7 km for an assumed distance of 6 kpc.

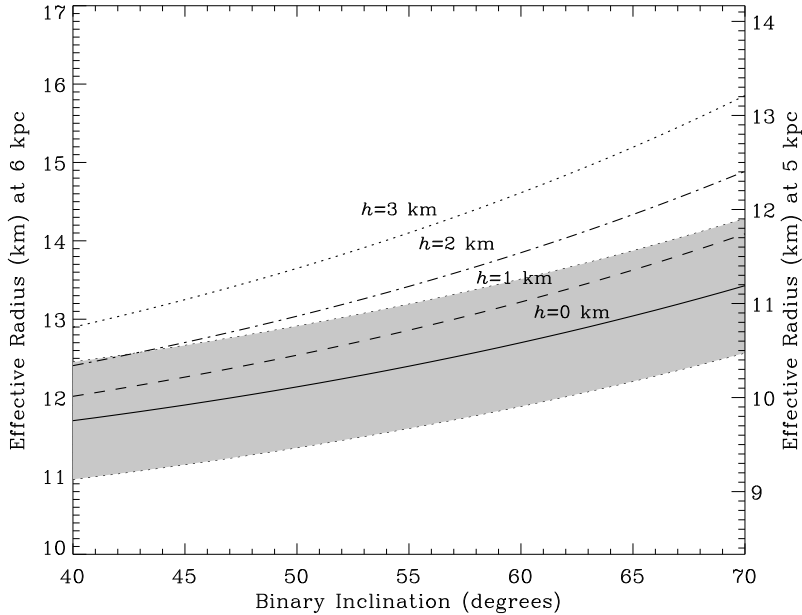


FIG. 6.— Effective stellar radius as a function of binary inclination and disk half-height (h) for source distances of 6 kpc (left axis) and 5 kpc (right axis). The shaded region represents the uncertainty and corresponds to the same range of blackbody radii as in Fig. 5. While the uncertainty is only plotted for $h = 0$, the magnitude of the uncertainties for the other values of h are approximately the same and have been omitted for clarity.

sured a burst recurrence time of 3.54 ± 0.03 hr, which is consistent with G04’s measurement. G04’s measured decrease in the burst recurrence time between 1997 and 2002 has been coupled with an even larger percentage increase in the mean persistent flux, possibly indicating that a greater fraction (as compared to 1997) of the stellar surface may be covered prior to ignition. We detected 611.2 Hz burst oscillations with a 0.033% chance that the signal resulted from random fluctuations. The average rms amplitude of the peak is 4.8%.

The *RXTE/Chandra* 0.5–200 keV integrated persistent emission spectrum is best fit with a dual Comptonization

model, whereby two distinct Comptonizing regions exist and are characterized by a different set of parameters. The extended energy range of *RXTE* is essential to constraining the photon index or Comptonization parameter, and eliminates the need for a blackbody component. This result is contrary to most spectral models of LMXBs that include a visible blackbody component. The spectrum also requires a neutral Fe K α emission line at 6.45 keV with EW ~ 37.2 eV. In addition, we find strong evidence of interstellar Fe L absorption features at the about 17.15 Å and 17.5 Å, with significance 3.8σ and 2.9σ , respectively.

During a burst, blackbody emission accounts for the majority of the flux though it quickly disappears after ~ 150 s. Throughout this period, the data are consistent with a blackbody radius between 10.3 km and 11.7 km for a distance of 6 kpc if one assumes the blackbody flux comes from the full $4\pi R^2$ of the neutron star surface. By accounting for the fraction of the surface that is obscured by the accretion disk, however, the source distance must be nearer to 5 kpc to be consistent with a neutron star radius of 10–12 km. We also see Compton cooling during the bursts, as the plasma temperature immediately decreases to ~ 3 keV and then slowly returns to the persistent emission value of ~ 6.8 keV after about 150 s. Since blackbody emission is not observed in the persistent spectrum yet dominates the burst spectrum, we conclude that the emission from those regions of the stellar surface along the equator are covered in the persistent phase. During the burst the entire surface is radiating as a blackbody, and so this

emission can be seen outside of the covered region.

We gratefully acknowledge support from NASA grants NAS5-30702 and GO2-3060X. We thank Tod Strohmayer for identifying a mistake we initially made when creating power spectra in the search for burst oscillations, and Lev Titarchuk for useful information regarding his `comptt` model in XSPEC. We also appreciate the input given by Jörn Wilms, and many comments and suggestions by the referee which significantly improved this paper. This research made use of data from the High Energy Astrophysics Science Archive Research Center Online Service, provided by the NASA/Goddard Space Flight Center. The analysis of the *Chandra* data made extensive use of the Chandra Interactive Analysis of Observations (CIAO), <http://cxc.harvard.edu/ciao>.

REFERENCES

- Balucińska-Church, M., Barnard, R., Church, M. J., & Smale, A. P. 2001, *A&A*, 378, 847
 Barret, D., Motch, C., & Pietsch, W. 1995, *A&A*, 303, 526
 Barret, D., Olive, J. F., Boirin, L., Done, C., Skinner, G. K., & Grindlay, J. E. 2000, *ApJ*, 533, 329
 Bildsten, L. 2000, preprint (astro-ph/0001135)
 Boirin, L., Méndez, M., Díaz Trigo, M., Parmar, A. N., & Kaastra, J. S. 2005, *A&A*, 436, 195
 Canizares, C. R., 1976, *ApJ*, 207, L101
 Canizares, C. R., Dewey, D., Galton, E. B., Markert, T. H., Smith, H. I., Schattenburg, M. L., Woodgate, B. E., & Jordan, S. 1992, in AIAA Conf. Proc.: Space Programs and Technologies, 11
 Church, M. J., Dotani, T., & Balucińska-Church, M. 1997, *ApJ*, 491, 388
 Church, M. J., Parmar, A. N., Balucińska-Church, M., et al. 1998, *A&A*, 338, 556
 Church, M. J. 2001, *Adv. Space Res.*, 28, 323
 Church, M. J., & Balucińska-Church, M. 2001, *A&A*, 369, 915
 Cocchi, M., Bazzano, A., Natalucci, L., Ubertini, P., Heise, J., in 't Zand, J. J. M., Müller, J. M., & Smith, M. J. S. 2000, AIP Conference Proceedings, 510, 203
 Crosby, N., Vilmer, N., Lund, N., & Sunyaev, R. 1998, *A&A*, 334, 299
 Cumming, A., & Bildsten, L. 2000, *ApJ*, 544, 453
 Del Sordo, S., et al. 1999, *Astrophys. Lett.*, 38, 125
 Dickey, J., & Lockman, F. 1990, *ARA&A*, 28, 215
 Draine, B. T. 2003, *ApJ*, 598, 1026D
 Ebisuzaki, T., Hanawa, T., & Sugimoto, D. 1984, *PASJ*, 36, 551
 Fender, R. P. 2002, in Relativistic Flows in Astrophysics:, eds. A. W. Guthmann, M. Georgopoulos, Macrowith, A., & Manolakou, K. (Heidelberg: Springer)
 Frank, J., King, A., & Raine, D. 1992, in Accretion Power in Astrophysics (2d ed; New York: Cambridge Univ. Press), 73
 Galloway, D. K., Cumming, A., Kuulkers, E., Bildsten, L., Chakrabarty, D., & Rothschild, R. E. 2004, *ApJ*, 601, 466 (G04)
 Garmire, G. P., Bautz, M. W., Ford, P. G., Nousek, J. A., & Ricker, G. R., Jr. 2003, *Proc. SPIE*, 4851, 28
 Homer, L., Charles, P. A., O'Donoghue, D. 1998, *MNRAS*, 298, 497
 in 't Zand, J. J. M., Heise, J., Kuulkers, E., Bazzao, A., Cocchi, M. & Ubertini, P. 1999(a), *A&A*, 347, 891
 in 't Zand, J. J. M., et al. 1999(b), *A&A*, 345, 100
 Inogamov, N. A., & Sunyaev, R. A. 1999, *Astron. Lett.*, 25, 269
 Jahoda, K., Swank, J. H., Giles, A. B., Stark, M. J., Strohmayer, T., Zhang, W., & Morgan, E. H. 1996, *Proc. SPIE*, 2808, 59
 Kong, A. K. H., Homer, L., Kuulkers, E., Charles, P. A., & Smale, A. P. 2000, *MNRAS*, 311, 405
 Kortright, J. B., & Kim, S.-K. 2000, *Phys. Rev. B*, 62, 12216
 Kreykenbohm, I., Wilms, J., Coburn, W., Kuster, M., Rothschild, R. E., Heindl, W. A., Kretschmar, P., & Staubert, R. 2004, *A&A*, 427, 975
 Leahy, D. A., et al. 1983, *ApJ*, 266, 160
 Lewin, W. H. G., van Paradijs, J., & Taam, R. E. 1995, in X-Ray Binaries, eds: W. H. G. Lewin, J. van Paradijs, & E. P. J. van den Heuvel, (Cambridge: Cambridge Univ. Press), 175
 London, R. A., Taam, R. E., & Howard, W. M. 1986, *ApJ*, 306, 170
 Madej, J., Joss, P. C., & Różańska, A. 2004, *ApJ*, 602, 904
 Makino, R., et al., 1988, *IAU Circ.*, 4653
 Marshall, H. L., Rothschild, R. E., & Heindl, W. A. 2003, in AAS HEAD meeting, 7, 17.35
 Mescheryakov, A. V., et al. 2004, *Astron. Lett.*, 30, 751
 Miller, J. M., et al. 2002, *ApJ*, 578, 348
 Mitsuda, K., Inoue, H., Nakamura, N., & Tanaka, Y. 1989, *PASJ*, 41, 97
 Munoz, M. P. 2004, in AIP Conf. Proc. 714: X-ray Timing 2003: Rossi and Beyond, 239
 Predehl, P., & Schmitt, J. 1995, *A&A*, 293, 889
 Protassov, R., van Dyk, D. A., Connors, A., Kashyap, V. L., & Siemiginowska, A. 2002, *ApJ*, 571, 545
 Rothschild, R. E., et al. 1998, *ApJ*, 496, 538
 Schulz, N. S., Cui, W., Canizares, C. R., Marshall, H. L., Lee, J. C., Miller, J. M., & Lewin, W. H. G. 2002, *ApJ*, 565, 1141
 Smale, A. P., Church, M. J., & Balucińska-Church, M. 2001, *ApJ*, 550, 962
 Spitkovsky, A., Levin, Y., & Ushomirsky, G. 2002, *ApJ*, 566, 1018
 Strickman, M., Skibo, J., Purcell, W., Barret, D., & Motch, C. 1996, *A&AS*, 120, 217
 Strohmayer, T., & Bildsten, L. 2003, in Compact Stellar X-Ray Sources, ed. W. H. G. Lewin & M. van der Klis (Cambridge: Cambridge Univ. Press)
 Tanaka, Y. 1989, in Proc. 23rd ESLAB Symp., Two Topics in X-Ray Astronomy, ed. J. Hunt & B. Battwick (SP-296; Noordwijk: ESA), 3
 Thompson, T. W. J., Rothschild, R. E., & Tomscik, J. A. 2005, in preparation
 Titarchuk, L. 1994, *ApJ*, 434, 570
 Ubertini, P. et al. 1997, *IAU Circ.*, 6611
 Ubertini, P., Bazzano, A., Cocchi, M., Natalucci, L., Heise, J., Müller, J. M., in 't Zand, J. J. M. 1999, *ApJ*, 514, L27
 Wallace & Woosley, 1981, *ApJS*, 45, 389
 Wilms, J., Allen, A., & McCray, R. 2000, *ApJ*, 542, 914
 Woosley, S. E., et al. 2004, *ApJ*, 151, 75
 Yoshida, K., Mitsuda, K., Ebisawa, K., Ueda, Y., Fujimoto, R., & Yaqoob, T. 1993, *PASJ*, 45, 605